

Influence of corner angle in streamwise supersonic corner flow

Yang, Rui; Modesti, Davide; Zhao, Yu Xin; Wang, Qian Cheng; Wang, Zhen Guo; Pirozzoli, Sergio

DOI

[10.1063/5.0046716](https://doi.org/10.1063/5.0046716)

Publication date

2021

Document Version

Final published version

Published in

Physics of Fluids

Citation (APA)

Yang, R., Modesti, D., Zhao, Y. X., Wang, Q. C., Wang, Z. G., & Pirozzoli, S. (2021). Influence of corner angle in streamwise supersonic corner flow. *Physics of Fluids*, 33(5), Article 056108. <https://doi.org/10.1063/5.0046716>

Important note

To cite this publication, please use the final published version (if applicable). Please check the document version above.

Copyright

Other than for strictly personal use, it is not permitted to download, forward or distribute the text or part of it, without the consent of the author(s) and/or copyright holder(s), unless the work is under an open content license such as Creative Commons.

Takedown policy

Please contact us and provide details if you believe this document breaches copyrights. We will remove access to the work immediately and investigate your claim.

Influence of corner angle in streamwise supersonic corner flow

Cite as: Phys. Fluids **33**, 056108 (2021); <https://doi.org/10.1063/5.0046716>

Submitted: 05 February 2021 . Accepted: 07 April 2021 . Published Online: 13 May 2021

 Rui Yang (杨瑞),  Davide Modesti,  Yu-xin Zhao (赵玉新),  Qian-cheng Wang (王前程), Zhen-guo Wang (王振国), and Sergio Pirozzoli



View Online



Export Citation



CrossMark

ARTICLES YOU MAY BE INTERESTED IN

[Mechanism of stabilization of porous coatings on unstable supersonic mode in hypersonic boundary layers](#)

Physics of Fluids **33**, 054105 (2021); <https://doi.org/10.1063/5.0048313>

[Unsteady shock interaction mechanisms of high enthalpy reacting flows over double wedges at Mach 7](#)

Physics of Fluids **33**, 056110 (2021); <https://doi.org/10.1063/5.0050202>

[Supersonic mode in a low-enthalpy hypersonic flow over a cone and wave packet interference](#)

Physics of Fluids **33**, 054104 (2021); <https://doi.org/10.1063/5.0048089>

Physics of Fluids

SPECIAL TOPIC: Tribute to
Frank M. White on his 88th Anniversary

SUBMIT TODAY!



Influence of corner angle in streamwise supersonic corner flow

Cite as: Phys. Fluids **33**, 056108 (2021); doi: 10.1063/5.0046716

Submitted: 5 February 2021 · Accepted: 7 April 2021 ·

Published Online: 13 May 2021



View Online



Export Citation



CrossMark

Rui Yang (杨瑞),¹  Davide Modesti,²  Yu-xin Zhao (赵玉新),^{1,a)}  Qian-cheng Wang (王前程),^{1,b)} 
Zhen-guo Wang (王振国),¹ and Sergio Pirozzoli³

AFFILIATIONS

¹Science and Technology on Scramjet Laboratory, College of Aerospace Science and Engineering, National University of Defense Technology, Changsha, Hunan 410073, China

²Aerodynamics Group, Faculty of Aerospace Engineering, Delft University of Technology, Kluyverweg 2, Delft 2629, The Netherlands

³Dipartimento di Ingegneria Meccanica e Aerospaziale, Sapienza Università di Roma, Roma 00184, Italy

^{a)}Author to whom correspondence should be addressed: zhaoyuxin@nudt.edu.cn

^{b)}Electronic mail: wqc1235@163.com

ABSTRACT

We use the Reynolds-averaged Navier–Stokes (RANS) equations with a full Reynolds stress model (RSM) to study the effect of the corner angle in supersonic corner flow. RANS data are compared to reference direct numerical simulation of fully developed a square duct flow, which support predictive capability of secondary flows from Stress- ω RSM. We then carry out a parametric study by changing the corner angle in the range $\theta = 45^\circ$ – 135° , focusing on the effect on the mean streamwise and secondary flow. The maximum strength of the secondary flows of about $0.015u_\infty$ occurs for $\theta = 90^\circ$, which is similar to what is found in fully developed square ducts. Secondary eddies have approximately unit aspect ratio, and they maintain their shape for different corner angles by translating in the direction parallel to the closest wall. As a result, the position of the vortex center can be described by a simple geometrical transformation of the wall-parallel coordinate. We find that small corner angles are responsible for locally relaminarization flow at the corner, but otherwise the mean streamwise velocity profiles transformed according to van Driest following the canonical law-of-the-wall.

Published under license by AIP Publishing. <https://doi.org/10.1063/5.0046716>

I. INTRODUCTION

Flows past streamwise corners formed by the intersection of two plates are common in aerospace applications, typical examples being aircraft wing–body junction, rectangular air intakes, and turbine-hub flow. Streamwise corner flows are characterized by the presence of secondary currents in cross-stream planes, which are driven by the normal and secondary-shear components of the Reynolds stress tensor.²³ Hence, they are commonly referred to as turbulent secondary flows, or corner vortices. Secondary flows typically come in the form of two counter-rotating eddies, which bring high-momentum fluid from the edge of the boundary layer toward the corner, with a maximum intensity of about $O(1\%u_\infty)$.¹⁹

Turbulent secondary flows were first studied in the low-speed regime by Prandtl,²⁴ who hypothesized their existence to explain the bulging of the mean streamwise velocity isolines toward the corner in square duct flow. Visualizations in support of this hypothesis were first provided by Nikuradse.¹⁹ Bragg¹ carried out experiments of boundary layer flow over a streamwise corner with 90° angle and used the

bulging of the velocity isolines as supporting evidence of secondary currents, although direct measurement of the cross-stream velocity components was not possible.

The study of turbulent secondary velocities in spatially developing corner flows involves additional numerical and experimental challenges as compared to fully developed noncircular ducts. For this reason, fully developed turbulent square duct flow is often the preferred prototype for studying secondary flows, based on the assumption that the structure and intensity of secondary flows is not affected by boundary layer growth.²⁰ This assumption has generally been confirmed by early experimental studies. For instance, Kornilov and Kharitonov⁸ reported secondary flow intensity of 2.5 – $3.5\%u_\infty$ for corner flow, as compared to 1 – $2\%u_b$ reported by Gessner and Jones⁷ for fully developed square duct flow, where u_∞ and u_b are the free-stream and bulk flow velocities, respectively.

More accurate measurements of secondary flows have been possible in recent years owing to direct numerical simulation (DNS) and access to high-performance computing resources. Pirozzoli *et al.*²³ and

Modesti *et al.*¹⁷ carried out DNS of the fully developed incompressible square duct flow and showed that their intensity is 1–2% u_b . As a result, the effect of secondary flows on the primary flow is weak, and the streamwise flow can be characterized as given by the superposition of independent wall flows on each side of the duct.

In the high-speed regime, flows over streamwise corners have been extensively studied for their relevance in supersonic air intakes^{3,4} and for their propensity to promote laminar-to-turbulent transition.²⁸ Davis and Kerlick⁴ and Davis and Gessner³ investigated supersonic developing adiabatic flow at inlet Mach number $M_\infty = u_\infty/c_\infty = 3.91$ (where c_∞ are the free-stream sound speed) and unit Reynolds number $Re_\infty/m = u_\infty/\nu_\infty = 1.8 \times 10^6/m$ (where ν_∞ is the free-stream kinematic viscosity). No significant compressibility effect on the secondary flows was reported, and it was found that the wall-normal van Driest-transformed velocity profiles still follow the universal law-of-the-wall. Morajkar *et al.*¹⁸ carried out experiments of supersonic corner flow using particle image velocimetry, basically confirming the findings of Davis and Kerlick.⁴ Modesti *et al.*¹⁶ carried out direct numerical simulation of developed flow in an isothermal square duct up to bulk Mach number $M_b = u_b/c_w = 3$ (where c_w is the speed of sound at the wall) and showed that secondary flows are not affected by compressibility as the cross-flow is largely subsonic. Those authors also showed that, in the supersonic regime, the streamwise flow can be viewed as the superposition of four concurrent walls; hence, classical compressibility transformations^{5,31} can be extended to multiple walls. As for the effect of Reynolds number on secondary flow intensity, DNS data of incompressible and supersonic square duct flow seem to suggest a scaling with the bulk flow velocity,^{16,23} at least within the limited Reynolds number range affordable by DNS. On the contrary, incompressible and supersonic Reynolds-averaged Navier–Stokes (RANS) with eddy-viscosity models and experiments^{13,29} seem to suggest scaling with the friction velocity.

Although a considerable amount of work has been carried out for secondary flows in fully developed and in corner flows, only a few studies have considered the effect of the corner angle, most limited to the low-speed regime. Eckert and Irvine⁶ carried out experiments in fully developed incompressible triangular ducts with corner angle 11.5° and reported laminar flow close to the corner. Daschiel *et al.*² carried out a direct numerical simulation of triangular ducts with corner angles 11.5° and 4°, finding laminar flow in the proximity of sharp corners, resulting in a lower friction as compared to ducts with the same hydraulic diameter. Raiesi *et al.*²⁵ carried out DNS of fully developed skewed ducts and also reported laminar flow at sharp corners.

In this study, we consider supersonic flow in a streamwise-aligned corner for free-stream Mach number $M_\infty = 2.95$, and unit Reynolds number $Re_\infty/m = 8.095 \times 10^6$. We have carried out RANS simulations by changing the corner angle in the range $\theta = 45^\circ$ – 135° to elucidate the effects on the mean streamwise flow and on the spatial development of the secondary flows.

II. NUMERICAL STRATEGY

A. Numerical method

Streamwise corner flow is here numerical analyzed using the Reynolds-averaged Navier–Stokes as physical model. It is well known that classical linear eddy-viscosity models have intrinsic problems in capturing secondary flows,³⁰ which is due to the anisotropy turbulence in the corner.²¹ This problem can be circumvented through the use of nonlinear constitutive relations.¹⁵ The quadratic constitutive relation

(QCR) shows potential ability in capturing secondary flow,²⁹ although there is still a gap between the predicted result and the experiment.¹² In this study, we use the Reynolds stress model of Wilcox³³ (Stress- ω RSM). Yang *et al.*³⁴ carried out RANS simulations of a supersonic square duct using the Stress- ω RSM model and confirmed its ability to accurately reproduce secondary flows. The RSM model involves a solution of the transport equation for the Reynolds stress tensor,

$$\begin{aligned} & \underbrace{\frac{\partial}{\partial t}(\overline{\rho u'_i u'_j})}_{\text{Local Time Derivative}} + \underbrace{\frac{\partial}{\partial x_k}(\overline{\rho \bar{u}_k u'_i u'_j})}_{C_{ij} \equiv \text{Convection}} \\ &= - \underbrace{\frac{\partial}{\partial x_k} \left[\overline{\rho u'_i u'_j u'_k} + p'(\delta_{kj} u'_i + \delta_{ik} u'_j) \right]}_{D_{T,ij} \equiv \text{Turbulent Diffusion}} \\ &+ \underbrace{\frac{\partial}{\partial x_k} \left[\overline{\mu \frac{\partial}{\partial x_k} (u'_i u'_j)} \right]}_{D_{L,ij} \equiv \text{Molecular Diffusion}} - \underbrace{\overline{\rho \left(u'_i u'_k \frac{\partial \bar{u}_j}{\partial x_k} + u'_j u'_k \frac{\partial \bar{u}_i}{\partial x_k} \right)}}_{P_{ij} \equiv \text{Stress Production}} \\ &+ \underbrace{p' \left(\frac{\partial u'_i}{\partial x_j} + \frac{\partial u'_j}{\partial x_i} \right)}_{\phi_{ij} \equiv \text{Pressure Strain}} - \underbrace{2\overline{\mu \frac{\partial u'_i}{\partial x_k} \frac{\partial u'_j}{\partial x_k}}}_{\varepsilon_{ij} \equiv \text{Dissipation}} \end{aligned} \quad (1)$$

where ρ and μ are the fluid density and dynamic viscosity, respectively; p is the pressure; and u_i is the velocity components. Reynolds decomposition is used, where the overline denotes ensemble averages and the prime superscript fluctuations thereof. The Reynolds stress transport equations are not closed, and terms like $D_{T,ij}$, ϕ_{ij} , and ε_{ij} require modeling.

The turbulent diffusion term is modeled after a standard linear eddy-viscosity ansatz,⁹

$$D_{T,ij} = \frac{\partial}{\partial x_k} \left(\frac{\mu_t}{\sigma_k} \frac{\partial \overline{u'_i u'_j}}{\partial x_k} \right), \quad (2)$$

where $\sigma_k = 0.82$, and the eddy viscosity is determined from $\mu_t = \bar{\rho} k / \omega$, with the turbulence kinetic energy k and the specific dissipation rate ω obtained from the baseline k – ω model.^{14,33}

As customary in most classical Reynolds stress models, the dissipation tensor is modeled as using the local isotropy hypothesis,

$$\varepsilon_{ij} = \frac{2}{3} (\bar{\rho} \varepsilon + \bar{\rho} \varepsilon M_t^2) \delta_{ij}, \quad (3)$$

where ε is the pseudo-dissipation, $M_t = \sqrt{2k}/\bar{c}$ is the turbulent Mach number, and \bar{c} is the local sound speed.²⁶

Correct modeling of the pressure–strain term is crucial for capturing secondary flows, because ϕ_{ij} redistributes energy across the normal Reynolds stresses, and this Reynolds stress anisotropy is one of the mechanisms responsible for secondary flows.¹⁵ Herein, the pressure–strain tensor is modeled after Wilcox,³³

$$\begin{aligned} \phi_{ij} = & -\frac{9}{5} \bar{\rho} \beta_{RSM}^* \omega \left[\overline{u'_i u'_j} - \frac{2}{3} \delta_{ij} k \right] - \hat{\alpha}_0 \left[P_{ij} - \frac{1}{3} P_{kk} \delta_{ij} \right] \\ & - \hat{\beta}_0 \left[D_{ij} - \frac{1}{3} P_{kk} \delta_{ij} \right] - k \hat{\gamma}_0 \left[S_{ij} - \frac{1}{3} S_{kk} \delta_{ij} \right], \end{aligned} \quad (4)$$

with model constants $\hat{\alpha}_0 = 213/275$, $\hat{\beta}_0 = 54/275$, $\hat{\gamma}_0 = 136/275$.

As in the standard $k-\omega$ model,³³ $\beta_{RSM}^* = \beta^* f_{\beta^*}$ is a correction factor given by

$$\beta^* = 0.09 \left(\frac{4/15 + (Re_t/12)^4}{1 + (Re_t/12)^4} \right) \left[1 + \frac{3}{2} F(M_t) \right], \quad (5)$$

where $Re_t = (\rho k)/(\mu\omega)$ is the turbulent Reynolds number, $F(M_t) = \max(M_t^2 - 0.25^2, 0)$, and

$$f_{\beta^*} = \begin{cases} 1 & \chi_k \leq 0, \\ \frac{1 + 640\chi_k^2}{1 + 400\chi_k^2} & \chi_k > 0, \end{cases} \quad \chi_k = \frac{1}{\omega^3} \frac{\partial k}{\partial x_j} \frac{\partial \omega}{\partial x_j}. \quad (6)$$

The modeled pressure-strain tensor (4) requires the term

$$D_{ij} = -\bar{\rho} \left[\overline{u'_i u'_m} \frac{\partial \bar{u}_m}{\partial x_j} + \overline{u'_j u'_m} \frac{\partial \bar{u}_m}{\partial x_i} \right], \quad (7)$$

and the mean rate-of-strain,

$$S_{ij} = 1/2 \left(\frac{\partial \bar{u}_j}{\partial x_i} + \frac{\partial \bar{u}_i}{\partial x_j} \right). \quad (8)$$

We numerically solve the RANS equations using a density-based coupled-implicit algorithm with Roe Riemann solver, whereby the Minmod limiter is used to reconstruct the conserved variables at the left and right cell interfaces. As customary for compressible flows, in the following we also use Favre averages ($\bar{\psi} = \bar{\rho\psi}/\bar{\rho}$).

B. Simulation Setup

Figure 1 shows a sketch of the computational setup for the streamwise corner flow. We carry out a parametric study changing the corner angle between $\theta = 45^\circ - 135^\circ$ in steps of 15° , for given free-stream Mach number and unit Reynolds number, namely $M_\infty = 2.95$ and $Re_\infty/m = 8.095 \times 10^6$. The computational domain is a circular cylindrical sector with streamwise length $L_x/\delta_{max} = 92.9$, where δ_{max} is the boundary layer thickness at the outflow, estimated using the empirical turbulent boundary layer thickness²⁷

$$\delta_s = 0.37x/Re_x^{1/5}. \quad (9)$$

The domain is divided into a corner zone and a buffer zone, as shown in Fig. 1(b). The corner zone has a diamond shape, with side length $L_c = 2\delta_{max}/\sin\theta$ inside which the mesh is refined, whereas the mesh is much coarser in the outer buffer zone and the total radius is $L_b = 8L_c$. As for the boundary conditions, we use nonreflecting conditions at the far field and no-slip adiabatic conditions at the wall. At the inflow, we consider a uniform flow and set the turbulence intensity to $I = 0.1\%u_\infty$. The inflow turbulence is assumed to be isotropic; thus, $\overline{u'_i u'_j} = 0$. The normal Reynolds stress component $\overline{u'^2} = \overline{v'^2} = \overline{w'^2} = 2/3k$, where turbulence kinetic energy $k = 3/2(u_\infty I)^2$. The specific dissipation rate $\omega = \rho_\infty k/\mu_\infty (\mu_t/\mu_\infty)^{-1}$, where the turbulent viscosity ratio μ_t/μ_∞ is set to 10 for typical external flow.

C. Verification and validation

A preliminary assessment of the RANS model has been carried out for the case of fully developed flow in a square duct, for which

DNS data are available, both for subsonic flow, and for supersonic flow. Subsonic reference DNS data²³ have bulk Mach number $M_b = 0.2$, bulk Reynolds number $Re_b = 2\rho_b u_b h/\mu_w = 40\,000$ (where h is the duct half side length, and ρ_b and μ_w are the bulk density and dynamic viscosity at the wall, respectively), and friction Reynolds number $Re_\tau^* = hu_\tau^*/\nu_w^* = 1055$, where $u_\tau^* = \sqrt{\tau_w^*/\rho_w^*}$ is mean the friction velocity, τ_w^* and ν_w^* are the mean wall shear stress and kinematic viscosity, the asterisk denoting averaging along the duct perimeter. The supersonic reference DNS case¹⁶ is at $M_b = 1.5$, $Re_b = 14\,600$, corresponding to friction Reynolds number $Re_\tau^* = 507$. We carried out RANS simulations of these two reference cases on a mesh with 121×121 grid points in the cross-stream plane and we impose a uniform body force driving the flow in the streamwise direction, thus matching the friction Reynolds number of the corresponding DNS. As a result, RANS simulations have bulk Mach numbers $M_b = 0.20$ and

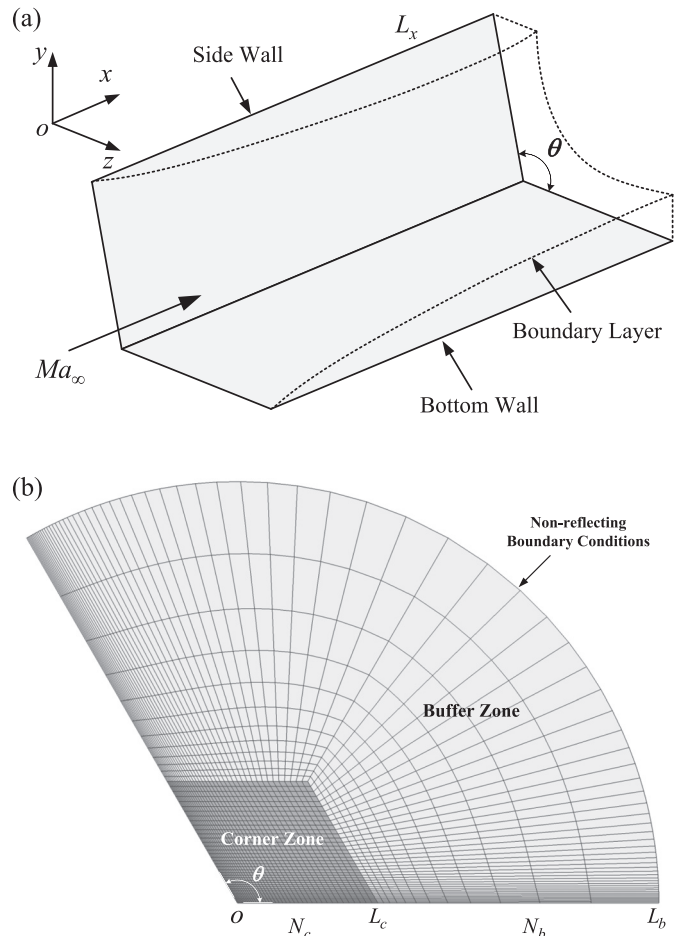


FIG. 1. (a) Sketch of the simulation setup and (b) computational mesh in a cross-stream section. θ is the corner angle, L_x is the streamwise length of the computational box, and M_∞ is the free-stream Mach number. The cross section is a circular sector with radius L_b , and the mesh is refined within a distance L_c from the corner. N_c and N_b are the number of mesh points in the corner zone (L_c) and the buffer zone ($L_b - L_c$), respectively.

$M_b = 1.55$, corresponding to bulk Reynolds numbers $Re_b = 40\,567$ and $Re_b = 15\,200$, respectively.

Figure 2 shows the mean streamwise \tilde{u}/u_τ^* and cross-stream velocities \tilde{v}/u_b for the subsonic [(a) and (c)] and for the supersonic [(b) and (d)] flow cases, compared with DNS data. In Figs. 2(a) and 2(b), the wall distance is normalized by the mean viscous length scale, $\delta_v^* = \nu_w^*/u_\tau^*$. Not unexpectedly, RANS correctly predicts the existence of mean velocity profiles with nearly logarithmic variation with the wall distance. It is certainly less expected that the Stress- ω RSM model is also capable of predicting the distribution and the intensity of the secondary motions, with a local error of no more than 10%. The cross-stream velocity contours shown in Fig. 3 further indicate that RANS is capable of predicting with good accuracy the topology and the intensity of the secondary motions; hence, it is also a good candidate to study the case of developing corner flow.

Having validated the model for fully developed flow, the mesh parameters for RANS of corner flows have been decided based on a grid convergence study, in which we have carried out at fixed corner angle ($\theta = 60^\circ$), using three meshes whose parameters are listed in

Table I. The computed streamwise and cross-stream velocity profiles at the station $Re_x = 1.618 \times 10^6$ are shown in Fig. 4. Here and elsewhere, the “+” superscript denotes quantities made nondimensional with respect to the local wall units, namely local friction velocity $u_\tau = \sqrt{\tau_w/\rho_w}$, and local viscous length scale, $\delta_v = \nu_w/u_\tau$. Following the analysis of Modesti *et al.*,¹⁶ we apply the classical van Driest velocity transformation in the direction normal to the closest wall (say y), at all x and z locations,

$$u_D(x, y, z) = \int_0^y \left(\frac{\bar{\rho}(x, \eta, z)}{\bar{\rho}_w(x, z)} \right)^{1/2} \frac{\partial \tilde{u}}{\partial \eta}(x, \eta, z) d\eta, \quad (10)$$

where $\bar{\rho}_w(x, z)$ is the mean density at the wall. The van Driest effective velocity profile at $Re_x = 1.618 \times 10^6$ away from the corner (see Fig. 4) is in good agreement with reference DNS data³² at matching free-stream Mach and Reynolds numbers, regardless of the mesh resolution. In Fig. 4(b), we also show the mean velocity profiles along the corner bisector as a function of the radial distance from the corner s/s_0 , where s_0 is the distance at which the radial velocity component \tilde{v} ,

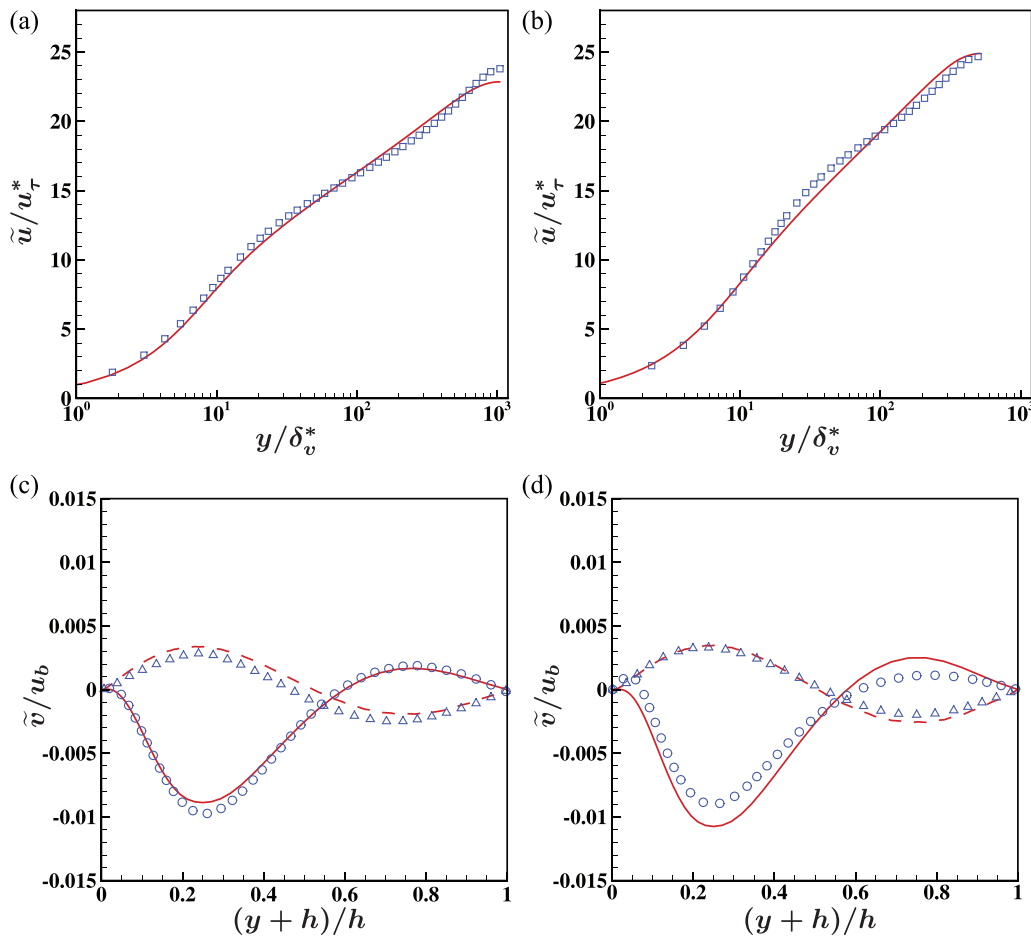


FIG. 2. Fully developed flow in a square duct: mean streamwise velocity profiles along the wall bisector [(a) and (b)], and mean cross-stream velocity [(c) and (d)] at $z/h = -0.75$ (solid), $z/h = -0.25$ (dashed). h is the half of the duct side length. The left column [panels (a) and (c)] shows a subsonic case at $Re_\tau^* = 1055$, and the right column [panels (b) and (d)] shows a supersonic case at $Re_\tau^* = 507$. The bulk Mach numbers are $M_b = 0.2$, $M_b = 1.5$ for DNS and $M_b = 0.20$, $M_b = 1.55$ for RANS. Symbols refer to DNS^{16,23} and lines to present RANS simulations.

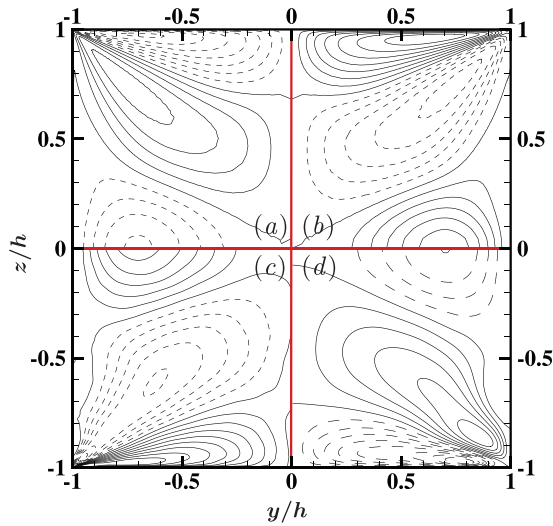


FIG. 3. Fully developed flow in a square duct: contours of mean cross-stream velocity. Contour levels are shown between $-0.016 \leq \bar{v}/u_b \leq 0.016$, in intervals of 0.002 (dashed lines denote negative values). The left column [(a) and (c)] shows a subsonic case at $M_b = 0.20$ (a), $M_b = 0.2$ (c), $Re_\tau^+ = 1055$, and the right column [(b) and (d)] shows a supersonic case at $M_b = 1.55$ (b), $M_b = 1.5$ (d), $Re_\tau^+ = 507$. Panels [(a) and (b)] correspond to RANS, and panels [(c) and (d)] correspond to DNS.^{16,23}

changes sign. Good agreement of results obtained with the various meshes is again observed, and the magnitude of the secondary flow is about $1.5\%u_\infty$. All simulations predict the secondary flow to be confined within the boundary layer, with velocity pointing toward the corner, whereas outside the boundary layer cross-stream velocities change sign due to concurrent growth of the boundary layers on the side walls. Although the results obtained with Mesh B and Mesh C are nearly coincident, some minor difference is observed on Mesh A regarding the secondary flow. Hence, in an attempt to balance computational cost and fidelity, all simulations hereafter reported are carried out on computational meshes with the same number of points as Mesh B.

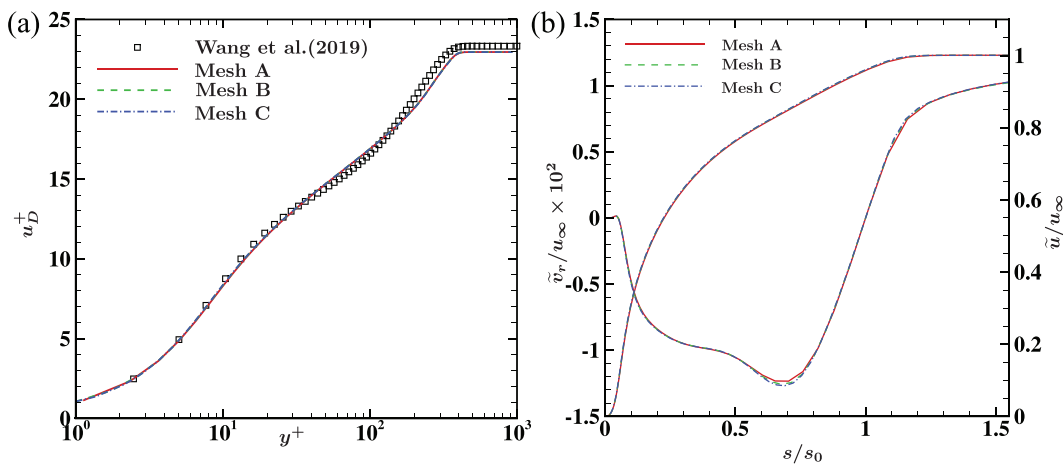


FIG. 4. Grid sensitivity study for $\theta = 60^\circ$: mean velocity profiles at $Re_x = 1.618 \times 10^6$. (a) Inner-scaled effective velocity profiles away from the corner, compared with DNS data of flat plate boundary layer from Ref. 32 at matching free-stream conditions, $M_\infty = 2.95$ and $Re_\infty/m = 8.095 \times 10^6$. The friction Reynolds number is $Re_\tau = 367.9$ for RANS and $Re_\tau = 361.4$ for DNS data. (b) Streamwise velocity (\tilde{u}) and velocity along the corner bisector (\tilde{v}_r) as a function of the radial distance from the corner s . s_0 is the radial distance at which \tilde{v}_r changes sign.

TABLE I. Mesh parameters for the grid refinement study at $\theta = 60^\circ$. N_x , N_c , and N_b are the number of grid points in the streamwise direction, the corner zone, and the buffer zone, respectively. $\Delta\eta_w^+$ is the maximum wall-normal mesh spacing, excluding the leading-edge region.

Mesh	N_x	N_c	N_b	N_{total}	$\Delta\eta_w^+$
A	211	61	15	1.17M	0.89
B	281	81	20	2.78M	0.68
C	351	101	25	5.42M	0.54

III. SECONDARY FLOWS

We first focus on the effect of θ on the secondary flows. To extract the vortex shape and position, we use the Liutex vortex detection method.^{10,11} The local vortex axis \mathbf{r} is defined as,

$$\nabla\mathbf{u} \cdot \mathbf{r} = \lambda_r \mathbf{r}, \tag{11}$$

where $\nabla\mathbf{u}$ is the velocity gradient tensor, and λ_r is its real eigenvalue. The vortex intensity is,

$$R = \boldsymbol{\omega} \cdot \mathbf{r} - \sqrt{(\boldsymbol{\omega} \cdot \mathbf{r})^2 - 4\lambda_{ci}^2}, \tag{12}$$

where $\boldsymbol{\omega}$ is the vorticity vector, and λ_{ci} is the imaginary part of the first complex eigenvalue of $\nabla\mathbf{u}$.

Figure 5 shows the isosurfaces of Liutex vortex magnitude R for $\theta = 120^\circ$, which highlight both the corner vortices and leading-edge structures. We also recall that in open corner flow there are no shocks, except for the weak shocks emanating from the leading edge, and therefore, the isosurfaces of the corner vortices are smoother than in closed air intakes.³⁴

Figure 6 shows the vortex center (red line) for $\theta = 120^\circ$ together with the vortex magnitude R at four cross-stream planes, highlighting the growth of the vortices as the boundary layer grows downstream. In the following, we use the cross-stream plane D in Fig. 6, corresponding to $Re_x = 4.86 \times 10^6$, for the analysis of the mean flow statistics.

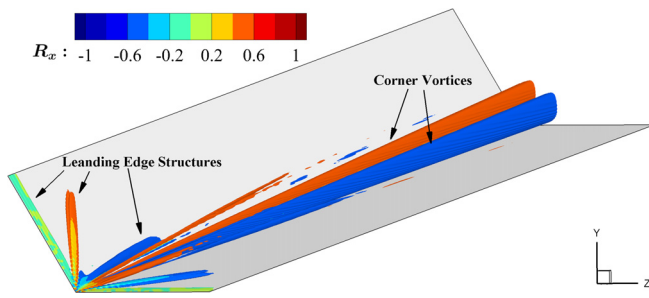


FIG. 5. Three-dimensional view of corner vortex structures for $\theta = 120^\circ$. Isosurfaces of the vortex strength $R = 0.5u_\infty/\ell_1$ are colored with the streamwise component of the Liutex vector, R_x [see Eq. (12)], and ℓ_1 is the unit length scale. $R_x > 0$ corresponds to clockwise vortex rotation.

The cross-stream flow topology is sketched in Fig. 7. Corner flows must be embedded inside the boundary layer, and for symmetry reasons, they cannot cross the vortex bisector. As a consequence, their distance from the closest wall (say y_{vc}) should be proportional to the local boundary layer thickness, and assuming (as is the case) that their core has $O(1)$ aspect ratio, their distance from the corner (say z_{vc}) should be inversely proportional to the corner angle. This expectation is confirmed from Fig. 8, where we show the vortex center coordinates as a function of Re_x , and scaled with the local boundary layer thickness δ far from the corner. We find in fact that wall distance of the vortex center does not depend on θ . On the other hand, we note the significant effect of the corner angle on the distance from the corner, which suggests that the vortex moves away from it as θ becomes smaller. In summary, we estimate that the vortex center coordinates at a given streamwise station should scale as

$$y_{fit}(x) = \alpha \delta_s(x), \tag{13a}$$

$$z_{fit}(x) = \alpha \delta_s(x) / \tan(\theta/\beta), \tag{13b}$$

which accounts for boundary layer growth as given from Eq. (9) and for change in the opening angle. Fitting RANS data shows that appropriate values of the fitting constants are $\alpha = 0.24$, $\beta = 4.75$. Figure 9 shows the coordinates of the vortex center scaled with respect to the predictions of Eq. (13). Significant deviations from the expected scaling are only observed for $\theta = 45^\circ$, as the flow in the corner region

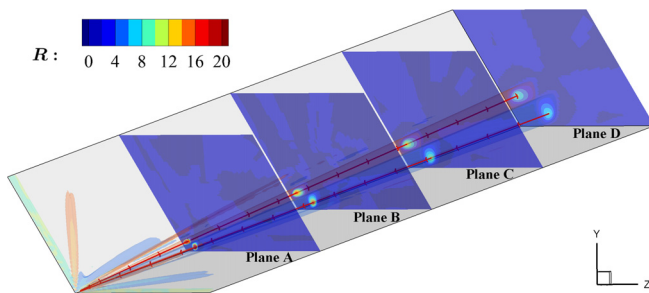


FIG. 6. Contours of vortex intensity (12) at four cross-stream planes, A: $Re_x = 1.214 \times 10^6$, B: $Re_x = 2.427 \times 10^6$, C: $Re_x = 3.641 \times 10^6$, and D: $Re_x = 4.86 \times 10^6$ and isosurfaces of the vortex intensity, for $\theta = 120^\circ$. The red lines indicate the vortex centers.

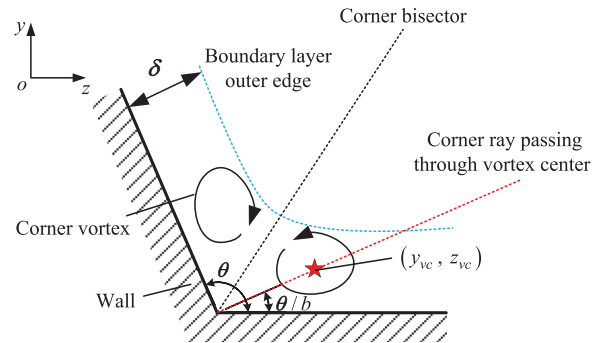


FIG. 7. Sketch of the corner vortex in the cross-stream plane. The red star symbol indicates the vortex center, θ is the corner angle and θ/β the angle at which the vortex center lies, with $\beta = 4.75$. δ is the local boundary layer thickness away from the corner.

tends to stay laminar, and for $\theta = 135^\circ$, at which corner vortices tend to be weaker, approaching the case of flat plate boundary layer.

Figure 9 supports our initial conjecture that corner vortices should have essentially unit aspect ratio; hence, their shape should be roughly independent of θ . To further check this assumption, in Fig. 10 we show isolines of the vortex magnitude, corresponding to $R = 0.5u_\infty/\ell_1$ (where ℓ_1 is the unit length scale) at Plane D, for different values of θ . As anticipated, we observe that the vortex core is displaced in the direction parallel to the bottom wall.

The strength of the secondary motions is quantified in Fig. 11, which shows the maximum value of the cross-stream velocity modulus \tilde{v}_{max} , as a function of Re_x . We find that the latter property ranges up to about $0.015u_\infty$, which is consistently with the value found in fully developed square duct flow.²³ In the range of flow parameters under scrutiny, we find that the secondary flow intensity is nearly independent of the Reynolds number, supporting the results of previous RANS simulations and experiments.^{13,29} We further note that \tilde{v}_{max}

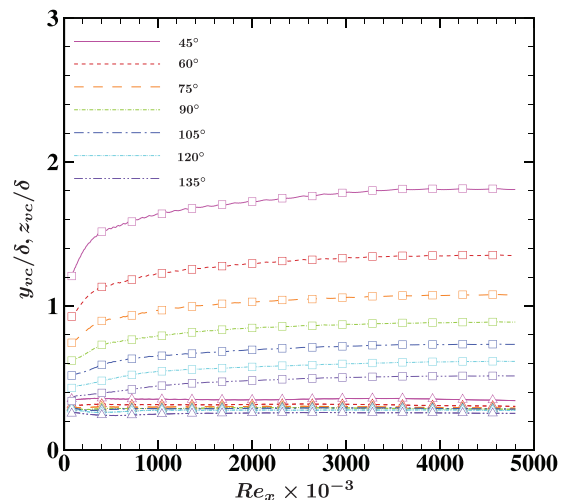


FIG. 8. Wall-normal (y_{vc} , \triangle) and wall-parallel (z_{vc} , \square) coordinates of corner vortex center as a function of Re_x , for different corner angles. δ is the local boundary layer thickness away from the corner. The arrow indicates increasing corner angle θ .

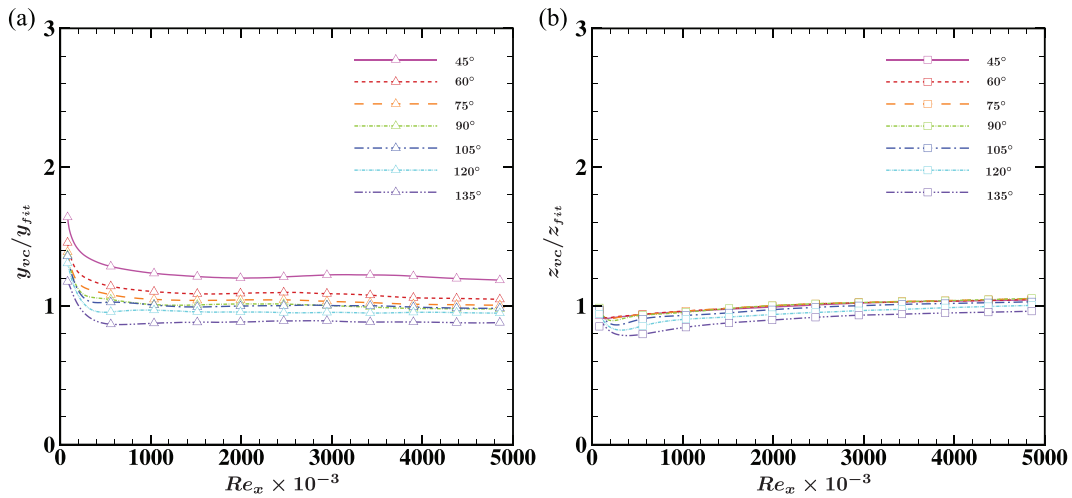


FIG. 9. Wall-normal (a) and wall-parallel (b) coordinates of the vortex center, normalized with respect to the predictions of Eq. (13), for various corner angles.

varies significantly with the corner angle, being minimum for $\theta = 135^\circ$ and $\theta = 45^\circ$. In the former case, this occurs because the flow approaches a flat plate boundary layer state, in which secondary eddies are not present, and in the latter because the flow tends to stay laminar for small corner angles. Furthermore, the amplitude of the cross-stream velocity change is different. When the angle decreases from $\theta = 90^\circ$, the cross-stream velocity decreases less than when the angle increases. So the velocity distributions are similar for $\theta = 75^\circ$ and $\theta = 90^\circ$.

IV. STREAMWISE VELOCITY

In order to gain a qualitative impression for the effect of corner angle variation on the primary, streamwise flow, in Fig. 12 we show velocity contours in the cross-stream plane D, along with cross-stream velocity vectors. Secondary flows come in the form of counter-rotating eddies bringing high-momentum fluid from the bulk, high-speed flow toward corners to compensate for reduced momentum. As a consequence, the boundary layer is distorted, and the velocity isolines tend to have a bulge near the corner, with the reduction in velocity at the outer edge of the corner eddies owing to the return, off-wall motion. Corner eddies have an influence on the distribution of the local friction coefficient, $C_f = 2\tau_w/(\rho_\infty u_\infty^2)$, which is shown as a function of z/δ in Fig. 13(a). For corner angles $\theta = 90^\circ-135^\circ$, the friction coefficient is nearly uniform away from corners, as it is expected to be.

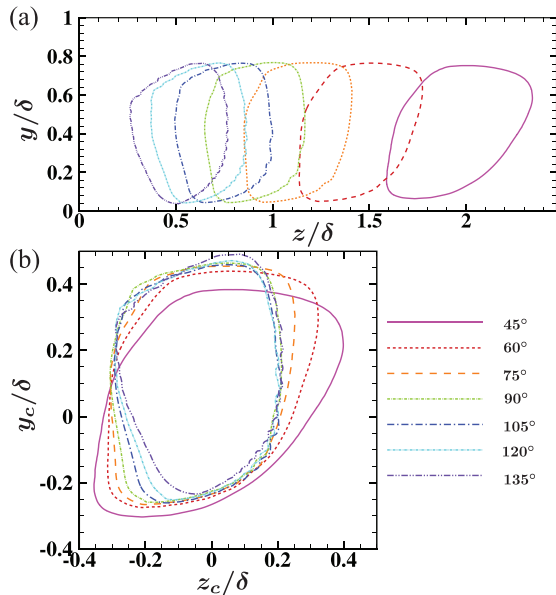


FIG. 10. Isolines of vortex intensity $R=0.5$ at plane D ($Re_x = 4.86 \times 10^6$): (a) untransformed coordinates and (b) shifted by the vortex center, $Z_c = Z - Z_{vc}$, $Y_c = Y - Y_{vc}$.

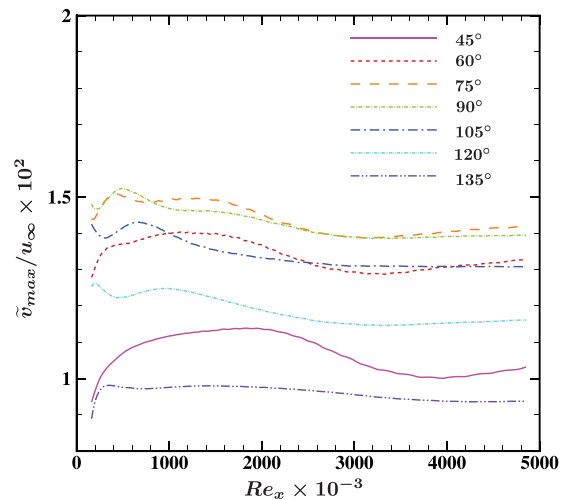


FIG. 11. Maximum of the cross-stream velocity as a function of Re_x for different corner angles.

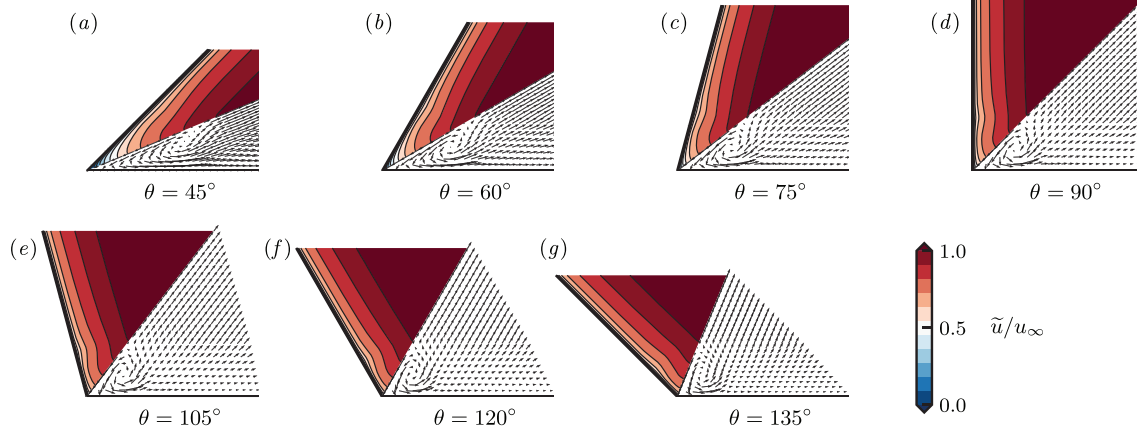


FIG. 12. Mean streamwise velocity contours (upper semi-corner) and cross-stream velocity vectors (lower semi-corner) at plane D for different corner angles (a) $\theta = 45^\circ$, (b) $\theta = 60^\circ$, (c) $\theta = 75^\circ$, (d) $\theta = 90^\circ$, (e) $\theta = 105^\circ$, (f) $\theta = 120^\circ$, and (g) $\theta = 135^\circ$. Velocity contours are shown in the range $0 \leq \tilde{u}/u_\infty \leq 1$ in intervals of 0.05. Velocity vectors are shown every eighth mesh point in each direction.

Moving toward the corner, C_f is obviously reduced, to a greater extent in the case of small corner angles, as a consequence of the previously noted tendency of the flow to stay laminar. A bulge in the C_f distribution is also observed at a distance increasing as θ is reduced narrower, which is associated with the outer boundary of the corner vortex. In fact, rescaling the z coordinate by z_{fit} yields near perfect collapse [see Fig. 13(b)].

Further evidence for relaminarization flow occurring at small corner angles is provided in Fig. 14, which shows profiles of the Reynolds shear stress $\bar{\rho} \tilde{u}'v' / \tau_{wfp}$ at all wall-parallel coordinates z , where τ_{wfp} is the wall shear stress away from the corner. Profiles at $z < z_{vc}$ are shown in red, and those at $z > z_{vc}$ in gray. We note a significant reduction in the turbulent shear stress as θ decreases, particularly for $\theta = 45^\circ$ and $\theta = 60^\circ$, consistently with the previously noted reduction of the friction coefficient for those cases.

Based on the above observations, in Fig. 15 we attempt to quantify the effect of the corner angle on the mean streamwise velocity distribution, by reporting the van Driest transformed velocity profiles for $Re_x = 4.86 \times 10^6$, at all z , up to the corner bisector. Velocity profiles taken at $z < z_{vc}$ are shown in red, and those at $z > z_{vc}$ in gray. For corner angles $\theta = 75^\circ - 135^\circ$ [panels (c)–(g)], the velocity profiles show a great deal of universality irrespective of the distance from the corner, closely matching the distributions found in flat plate boundary layers at matching Mach and Reynolds number.²² This interesting finding further strengthens claims made about the robustness of the law-of-the-wall, also outside the strict limits of its applicability.²³ However, a clear departure from universality is observed for $\theta = 45^\circ$ and $\theta = 60^\circ$ [panels (a) and (b)], at which the velocity profiles in the region occupied by the corner vortex ($z < z_{vc}$) clearly overshoot the log law, which again is a clear symptom of locally relaminarization flow.

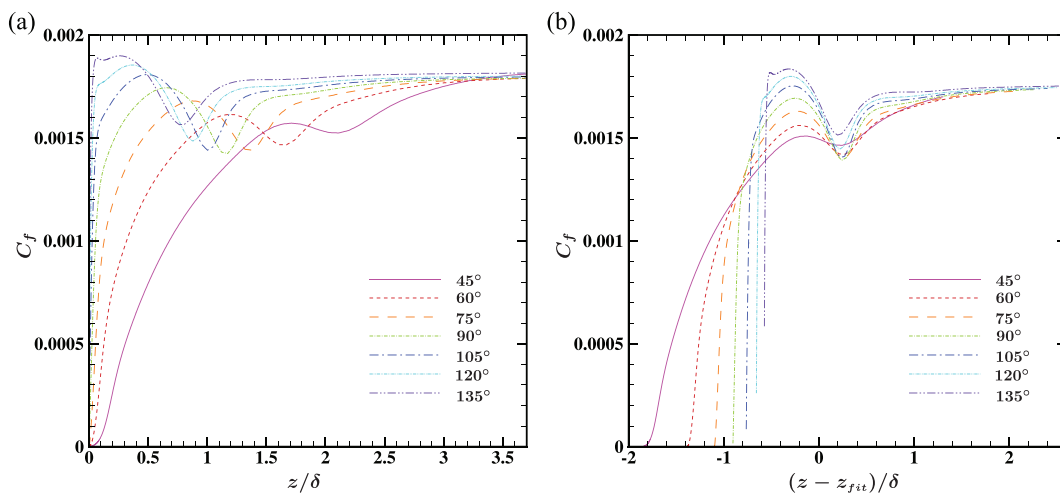


FIG. 13. Friction coefficient $C_f = 2\tau_w / (\rho_\infty u_\infty^2)$ as a function of the wall-parallel coordinate at plane D: (a) as a function of z/δ and (b) as a function of $(z - z_{fit})/\delta$. δ is the boundary layer thickness away from the sidewall, and z_{fit} is the coordinate of the fitted vortex center.

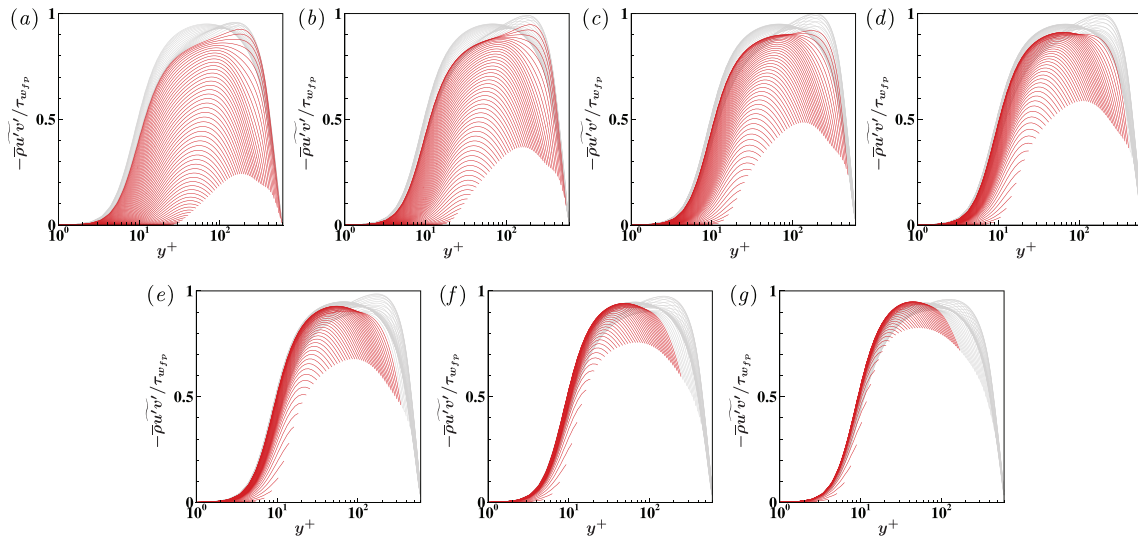


FIG. 14. Reynolds shear stress profiles $\bar{\rho}u'v' / \tau_{wfp}$ as a function of wall-normal coordinate, y^+ . Profiles are plotted at all wall-parallel coordinates z , up to the corner bisector, for different corner angles (a) $\theta = 45^\circ$, (b) $\theta = 60^\circ$, (c) $\theta = 75^\circ$, (d) $\theta = 90^\circ$, (e) $\theta = 105^\circ$, (f) $\theta = 120^\circ$, and (g) $\theta = 135^\circ$. τ_{wfp} is wall shear stress away from the corner.

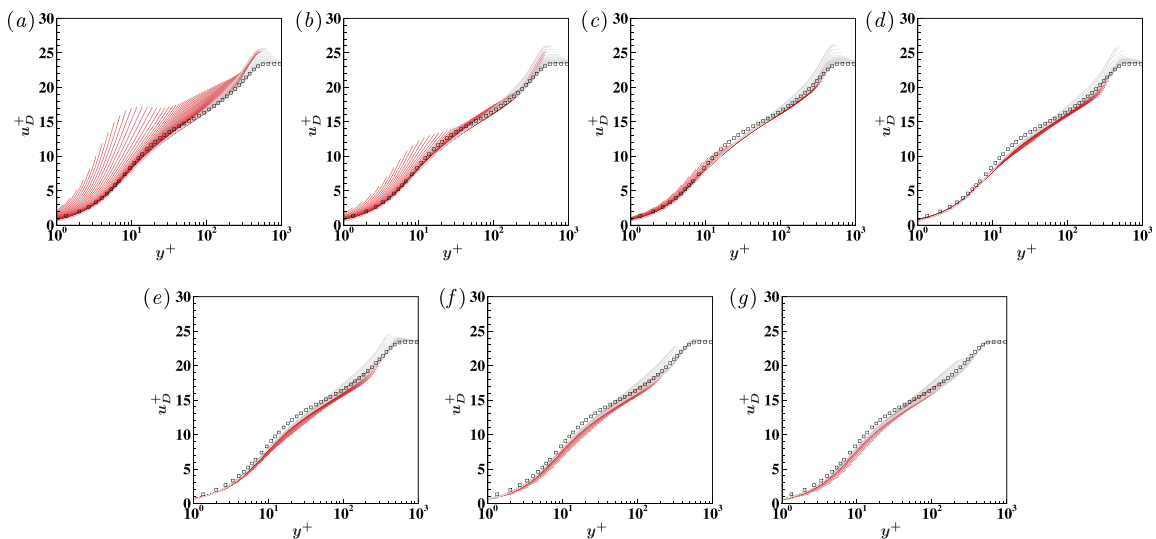


FIG. 15. Van Driest-transformed mean streamwise velocity $[u_D^+]$, see (10) as a function of wall-normal coordinate, y^+ . Profiles are plotted at all wall-parallel coordinates z , up to the corner bisector, for different corner angles (a) $\theta = 45^\circ$, (b) $\theta = 60^\circ$, (c) $\theta = 75^\circ$, (d) $\theta = 90^\circ$, (e) $\theta = 105^\circ$, (f) $\theta = 120^\circ$, and (g) $\theta = 135^\circ$. Square symbols denote DNS data of Pirozzoli and Bernardini²² for supersonic flat plate boundary layer at friction Reynolds number $Re_\tau = 500$ and free-stream Mach number $M_\infty = 3$.

V. CONCLUSIONS

We use the Stress- ω RSM to investigate the effect of corner angle in supersonic flows over streamwise corners, focusing on both the streamwise and secondary flow. Although RSM is known to improve the prediction of the Reynolds stress anisotropies, comparison with high-Reynolds number DNS data is much more scarce as compared to linear and nonlinear eddy-viscosity models. This is due to the notorious numerical issues of RSM as compared to eddy-viscosity models, namely numerical instabilities, lack of convergence, and, of course, additional computational cost, owing to the numerous transport

equations. For this reason, we carried out extensive validation of the turbulence model using recent DNS data of subsonic and supersonic fully developed square duct flow. We find that the Reynolds stress model accurately captures both the mean streamwise and secondary flow with errors smaller than 10% with respect to reference DNS data. Therefore, the Stress- ω RSM is also a good candidate to study the flow over streamwise corners and the spatial development of secondary flows for different corner angles.

We observe that corner vortices are confined by the boundary layer thickness $\delta_s(x)$ in the wall-normal direction and therefore their

distance from the closest wall does not depend on the corner angle, but only on $\delta_s(x)$.

On the other hand, their distance from the corner depends on θ and, decreasing the corner angle, the vortices move away from the corner in the direction parallel to the closest wall. Hence, the position of the vortex center can be described by a simple translation of the wall-parallel coordinate. The spanwise translation of the corner vortices can be traced back to the tendency of the vortex core to remain approximately isotropic, and therefore, the vortex maintains a unit aspect ratio.

The scaling of the secondary flow intensity with the Reynolds number is an unsettled topic, as DNS data²³ suggest scaling with the bulk flow (or free-stream) velocity, whereas RANS²⁹ data at higher Reynolds number support scaling with the friction velocity. The present data show independence of the secondary flow intensity from the Reynolds number, in agreement with previous RANS, although DNS data at higher Reynolds number would be necessary to fully support this scaling.

As for the effect of the corner angle on the secondary flow intensity, we find variations up to 50%. We observe the strongest secondary flow intensity ($\approx 0.015u_\infty$) for $\theta = 90^\circ$, whereas the weakest ($\approx 0.01u_\infty$) is observed for $\theta = 45^\circ$ and $\theta = 135^\circ$, the former because the flow close to the corner tends to stay laminar, the latter because the flow approaches a flat plate boundary layer.

Analysis of the friction coefficient and the turbulent shear stress shows that for small corner angles the flow tends to stay laminar in the region between the corner and the vortex center. Excluding this relaminarization flow region, the flow can be characterized as the superposition of two independent walls and the van Driest velocity profiles up to the corner bisector follow the canonical law-of-the-wall. RANS data show that the outer flow structure is rather insensitive to local variations of the wall-shear stress. Although the robustness of the outer layer similarity is a well-known feature of wall turbulence over complex wall patterns, such as roughness, this is certainly less obvious for the case of multiple walls and these findings contribute to strengthening the validity of the law-of-the-wall for complex geometries.

AUTHORS' CONTRIBUTIONS

All authors contributed equally to this work.

ACKNOWLEDGMENTS

We thank Professor Chao-qun Liu and Dr. Yi-sheng Gao for providing the program of vortex recognition. This work is funded by the National Natural Science Foundation of China (Grant No. 11802336).

The authors declare that they have no known competing financial interests or personal relationships that could have appeared to influence the work reported in this paper.

DATA AVAILABILITY

The data that support the findings of this study are available from the corresponding author upon reasonable request.

REFERENCES

- G. M. Bragg, "The turbulent boundary layer in a corner," *J. Fluid Mech.* **36**, 485 (1969).
- G. Daschiel, B. Frohnapfel, and J. Jovanović, "Numerical investigation of flow through a triangular duct: The coexistence of laminar and turbulent flow," *Int. J. Heat Fluid Flow* **41**, 27–33 (2013).
- D. Davis and F. Gessner, "Further experiments on supersonic turbulent flow development in a square duct," *AIAA J.* **27**, 1023–1030 (1989).
- D. O. Davis and G. D. Kerlick, "Experimental and numerical investigation of supersonic turbulent flow through a square duct," *AIAA J.* **24**, 1508–1515 (1986).
- E. R. van Driest, "Turbulent boundary layer in compressible fluids," *J. Aeronaut. Sci.* **18**, 145–160 (1951).
- E. R. G. Eckert and T. F. Irvine, "Flow in corners of passages with noncircular cross sections," *Trans. ASME* **78**, 709–718 (1956).
- F. Gessner and J. Jones, "On some aspects of fully-developed turbulent flow in rectangular channels," *J. Fluid Mech.* **23**, 689–713 (1965).
- V. Kornilov and A. Kharitonov, "Investigation of the structure of turbulent flows in streamwise asymmetric corner configurations," *Exp. Fluids* **2**, 205–212 (1984).
- F. Lien and M. Leschziner, "Assessment of turbulence-transport models including non-linear RNG eddy-viscosity formulation and second-moment closure for flow over a backward-facing step," *Comput. Fluids* **23**, 983–1004 (1994).
- C. Liu, Y. Gao, S. Tian, and X. Dong, "Rortex—A new vortex vector definition and vorticity tensor and vector decompositions," *Phys. Fluids* **30**, 035103 (2018).
- C.-q. Liu, Y.-s. Gao, X.-r. Dong, Y.-q. Wang, J.-m. Liu, Y.-n. Zhang, X.-s. Cai, and N. Gui, "Third generation of vortex identification methods: Omega and Liutex/Rortex based systems," *J. Hydrodyn.* **31**, 205–223 (2019).
- M. Mani, D. Babcock, C. Winkler, and P. Spalart, "Predictions of a supersonic turbulent flow in a square duct," in *51st AIAA Aerospace Sciences Meeting Including the New Horizons Forum and Aerospace Exposition, American Institute of Aeronautics and Astronautics, Grapevine (Dallas/Ft. Worth Region, Texas, 2013)*.
- C. K. McKenna, B. E. Rice, N. J. Bisek, S. J. Peltier, and J. W. Hofferth, "Reynolds number effects on secondary motion in corner flow boundary layers," in *AIAA Aviation 2019 Forum, 17–21 June 2019, Dallas, Texas* (ARC, 2019).
- F. Menter, "Two-equation eddy-viscosity turbulence models for engineering applications," *AIAA J.* **32**, 1598–1605 (1994).
- D. Modesti, "A priori tests of eddy viscosity models in square duct flow," *Theor. Comput. Fluid Dyn.* **34**, 713–734 (2020).
- D. Modesti, S. Pirozzoli, and F. Grasso, "Direct numerical simulation of developed compressible flow in square ducts," *Int. J. Heat Fluid Flow* **76**, 130–140 (2019).
- D. Modesti, S. Pirozzoli, P. Orlandi, and F. Grasso, "On the role of secondary motions in turbulent square duct flow," *J. Fluid Mech.* **847**, 1 (2018).
- R. R. Morajkar, J. F. Driscoll, and M. Gamba, "Experimental study of supersonic turbulent corner flow evolution in a low aspect ratio rectangular channel," *53rd AIAA Aerospace Sciences Meeting, 5–9 January 2015, Kissimmee, Florida* (ARC, 2015).
- J. Nikuradse, "Untersuchungen Über Die Geschwindigkeitsverteilung in Turbulenten Strömungen," Ph.D. thesis (Göttingen, 1926).
- P. Orlandi and S. Pirozzoli, "Transitional and turbulent flows in rectangular ducts: Budgets and projection in principal mean strain axes," *J. Turbul.* **21**, 1–25 (2020).
- P. Orlandi and S. Pirozzoli, "Turbulent flows in square ducts: Physical insight and suggestions for turbulence modellers," *J. Turbul.* **21**, 106–128 (2020).
- S. Pirozzoli and M. Bernardini, "Turbulence in supersonic boundary layers at moderate Reynolds number," *J. Fluid Mech.* **688**, 120–168 (2011).
- S. Pirozzoli, D. Modesti, P. Orlandi, and F. Grasso, "Turbulence and secondary motions in square duct flow," *J. Fluid Mech.* **840**, 631–655 (2018).
- L. Prandtl, "über die ausgebildete turbulenz" ("Investigations on turbulent flow"), in *International Congress for Applied Mechanics (ZAMM, 1926)*.
- H. Raiesi, A. Pollard, and U. Piomelli, "Direct numerical simulations of turbulence induced secondary motion in square and skewed ducts," in *Seventh International Symposium on Turbulence and Shear Flow Phenomena* (Begel House Inc., 2011).
- S. Sarkar and B. Lakshmanan, "Application of a Reynolds stress turbulence model to the compressible shear layer," *AIAA J.* **29**, 743–749 (1991).
- H. Schlichting and K. Gersten, *Boundary-Layer Theory* (Springer, 2016).

- ²⁸O. Schmidt and U. Rist, “Linear stability of compressible flow in a streamwise corner,” *J. Fluid Mech.* **688**, 569–590 (2011).
- ²⁹P. R. Spalart, A. Garbaruk, and A. Stabnikov, “On the skin friction due to turbulence in ducts of various shapes,” *J. Fluid Mech.* **838**, 369 (2018).
- ³⁰C. G. Speziale, “On turbulent secondary flows in pipes of noncircular cross-section,” *Int. J. Eng. Sci.* **20**, 863–872 (1982).
- ³¹A. Trettel and J. Larsson, “Mean velocity scaling for compressible wall turbulence with heat transfer,” *Phys. Fluids* **28**, 026102 (2016).
- ³²Q.-C. Wang, Z.-G. Wang, M.-B. Sun, R. Yang, Y.-X. Zhao, and Z. Hu, “The amplification of large-scale motion in a supersonic concave turbulent boundary layer and its impact on the mean and statistical properties,” *J. Fluid Mech.* **863**, 454–493 (2019).
- ³³D. C. Wilcox, *Turbulence Modeling for CFD*, 3rd ed. (Birmingham Press, California, 2006).
- ³⁴R. Yang, Z.-g. Wang, Y.-x. Zhao, Q.-c. Wang, and W.-h. Feng, “Numerical investigation on spatial development of the secondary flow in a supersonic turbulent square duct,” *Aerosp. Sci. Technol.* **100**, 105832 (2020).